Solar RRL
www.solar-rrl.com

Effect of Meso- or β-Functionalization of Porphyrins on the Photovoltaic Properties of Organic Solar Cells

Rubén Caballero, Rocío Domínguez, Shyam Shankar S., María Privado, Pilar Prieto, Pilar de la Cruz, Rahul Singhal, Ganesh D. Sharma,* and Fernando Langa**

Porphyrin derivatives are widely used as donors in organic solar cells (OSCs) due to their excellent optical and electrochemical properties. Although porphyrins can be functionalized at the meso- and β-positions, only meso-functionalized porphyrins have been reported as OSCs. Consequently, a direct comparison of the properties of porphyrins functionalized at these two positions is needed. The synthesis of two similar D–π–A–π–D materials is described herein and these compounds contain benzothiadiazole as the acceptor core and two Ni-porphyrins as donors functionalized at the meso- and β-positions to give RC19 and RC20, respectively. The optical and electrochemical properties of these compounds are reported. All-small-molecule OSCs based on RC19:TOCR1 and RC20:TOCR1 active layers show power conversion efficiencies (PCEs) of 13.72% and 5.20%, respectively. It should be noted that the PCE of 13.72% obtained for RC19:TOCR1 devices is, to one's knowledge, the highest value reported for porphyrin-based binary OSCs. The higher PCE obtained for RC19 is due to its higher photon harvesting ability, more efficient exciton dissociation and charge transfer, balanced charge transport, and lower bimolecular and trap-assisted recombination.

1. Introduction

The power conversion efficiency (PCE) of bulk-heterojunction (BHJ)-based organic solar cells (OSCs) depends on the design of donors and acceptors and this area has attracted significant attention owing to the low cost, flexibility, lightweight, semi-transparency, and simplicity of such devices.[1–7] The recent developments in nonfullerene acceptors (NFAs), particularly the Y6 series,[8–14] and device engineering and morphology have led to PCE values that exceed 19%[15–21] and 20%[22,23] for single-layer and tandem structures, respectively. All of these high-performance OSCs are based on conjugated polymers, which suffer from some limitations due to the uncertain molecular structures and batch-to-batch variations.[24–26] The former limitations have been addressed by using small-molecule donors (SMDs) as these offer notable advantages such as defined molecular structures, relatively simple synthesis and purification processes, and simple tailoring of the absorption and energy levels.[27–33] Recently, all-small-molecule OSCs (ASM-OSCs) have shown PCE values close to 17%,[34–40] which is very close to the values obtained for polymer-containing devices and highlights their potential commercial applications. In order to improve the PCE values of ASM-OSCs, it is necessary to develop new SMDs with appropriate absorption and energy levels.

The porphyrin ring is an archetypical planar aromatic macrocycle that can host a metal in the center and this system acts as a light harvester in photosynthesis, e.g., chlorophylls. This ring system has been extensively investigated in the OSC active layers (electron donor or acceptor) owing to its efficient electron transfer, broad absorption, and high absorption coefficient in the UV–vis region of the solar spectrum.[41–44] The porphyrin absorption range is around 400–450 nm in the Soret (blue) band and 500–650 nm in the Q (red) band region of the visible spectrum. These ranges can be easily extended to the near-infrared (NIR) region by using an acceptor–donor–acceptor or donor–acceptor–donor configuration in which the porphyrin is the donor core in the center or at the terminus. There are several efficient ways to tune the electronic properties of materials, and these include extending the π-conjugated backbone length, changing the end-capping moieties, or inserting different metal atoms into the central position of the porphyrin macrocycle, as well as

R. Caballero, R. Domínguez, M. Privado, P. de la Cruz, F. Langa
Universidad de Castilla-La Mancha
Instituto de Nanociencia
Nanotecnología y Materiales Moleculares (INAMOL)
Campus de la Fábrica de Armas, 45071 Toledo, Spain
E-mail: pilar.cruz@uclm.es; Fernando.Langa@uclm.es

S. S. S., G. D. Sharma
Department of Physics
The LNM Institute of Information Technology
Jamdoli, Jaipur, Rajasthan 302031, India
E-mail: gdsharma@lnmiit.ac.in

P. Prieto
Department of Organic Chemistry
Faculty of Chemical Sciences and Technologies-IRICA
University of Castilla-La Mancha
13071 Ciudad Real, Spain

R. Singhal
Department of Physics
Malviya National Institute of Technology
JLN Marg, Jaipur, Rajasthan 302017, India

G. D. Sharma
Department of Electronics and Communication Engineering
The LNM Institute of Information Technology
Jamdoli, Jaipur, Rajasthan 302031, India

The ORCID identification number(s) for the author(s) of this article can be found under https://doi.org/10.1002/solr.202400069.

DOI: 10.1002/solr.202400069

introducing different functional groups in the meso- or β-positions of the porphyrin. Intense research has been devoted to the development of effective porphyrin-based SMDs for OSCs owing to their advantageous optical and electrical properties.[45–53] Indeed, OSCs based on the BHJ active layer with porphyrin as a donor and non-fullerene small molecule acceptor (NFSMA) have provided record PCE values of 12.06%[54] and 16%[34] for binary and ternary structures, respectively. In all cases, the porphyrin macrocycle is linked to the conjugated backbone through the meso-position and the use of the β-position of the macrocycle to synthesize the donor–acceptor–donor or acceptor–donor–acceptor SMD has not been reported.

Organic semiconducting materials usually consist of a π-conjugated backbone that contains electron donors (D) alternated with electron acceptors (A). The development of appropriate D and A units is a reasonable approach to alter photophysical properties (optical and electrochemical), facilitate efficient carrier transport to obtain higher charge carrier mobility in organic semiconducting materials, and attain higher PCE values in the resultant OSCs.

Typically, SMs acting as electron donors exhibit an A–D–A structure. However, several studies reported in the literature demonstrate that D–A–D systems, utilized as electron donors in OSCs, yield good PCE values, sometimes even surpassing those of the conventional A–D–A structure.[52]

Besides, the 2,1,3-benzothiadiazole (BTDA) unit is considered to be a good electron acceptor in small-organic molecules for organic electronics due to its strong intramolecular charge transfer (CT). The BTDA benzene ring has four reactive sites than can be coupled with various conjugated units to build extended π-conjugated systems and this approach is widely employed in polymer donors, SMDs, and NFAs.[55–58] The use of BTDA as an acceptor can lead to a decrease in both highest occupied molecular orbital (HOMO) and lowest unoccupied molecular orbital (LUMO) energy levels and this, in turn, leads to intense light absorption and good photochemical stability, with this unit often coupled with a variety of electron-rich groups to form low bandgap polymers and SMs.[55]

Ni-porphyrins exhibit a HOMO energy level deeper than that of Zn-porphyrin-based systems. This characteristic results in improved V_{OC} values, leading to higher PCEs.[59,60]

The work described here concerns the design and synthesis of two D–π–A–π–Ds SMs that contain the same donor (Ni-porphyrin), thiophene (π-linkers), and core acceptor benzothiadiazole (BTDA). The difference between these SMs lies in the linking positions, i.e., the meso- and β-position of Ni-porphyrin for **RC19** and **RC20**, respectively. The optical and electrochemical properties were studied in depth to obtain information about the effect of the linking position on the absorption and frontier molecular orbitals. A NFA, namely, TOCR1,[61] was employed to produce devices and the optimized BHJ-OSCs fabricated under ambient conditions based on **RC19** and **RC20** (**Figure 1**) gave PCE values of 13.72% and 5.20%, respectively. It should be noted that 13.72% represents the highest efficiency reported to date for binary OSCs based on porphyrins (Figure S28 and Table S3, Supporting Information).

2. Results and Discussion

2.1. Synthesis of Porphyrin Donor Materials

The structures of **RC19** and **RC20** consist of a D–A–D architecture in which two nickel porphyrins act as donors and a BTDA acts as an acceptor with two 2,5-bis-ethynylthiophene linkers as π-spacers to connect the Ni-porphyrins and BTDA. The two D–A–D systems differ in the linking position of the porphyrin. In **RC20**, the porphyrin is linked through the β-position whereas in **RC19** the link is at the meso-position.

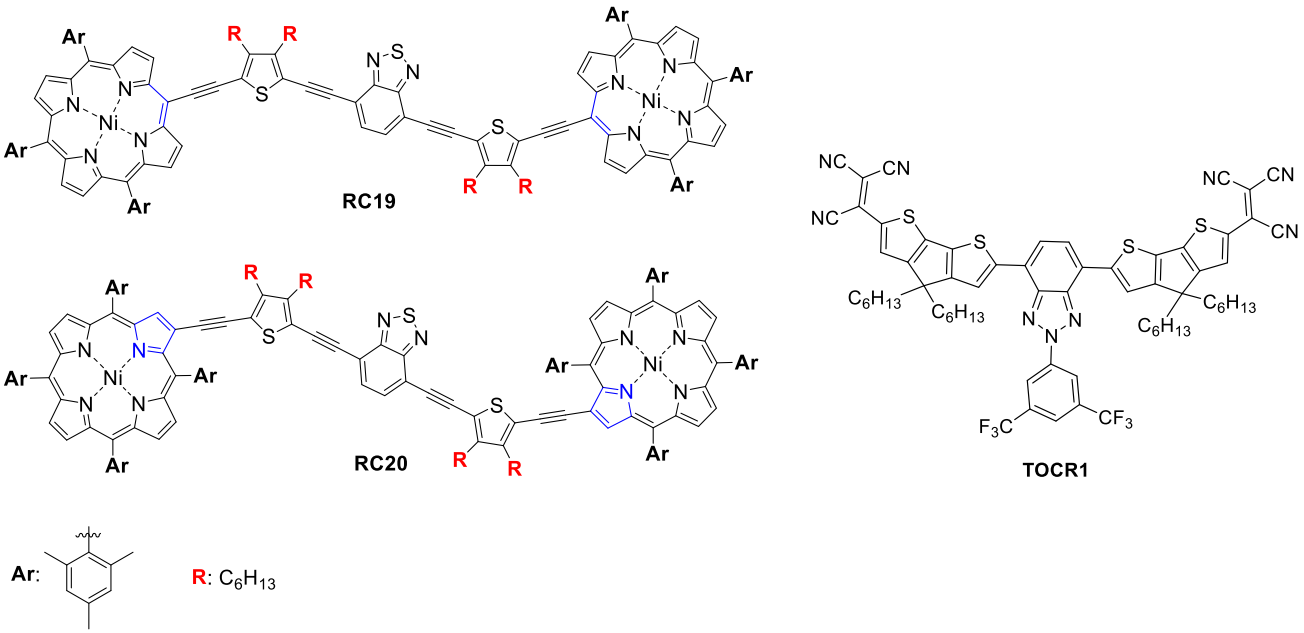

Figure 1. Structures of the target D–A–D systems based on porphyrins, namely, **RC19** and **RC20**, and the acceptor TOCR1.

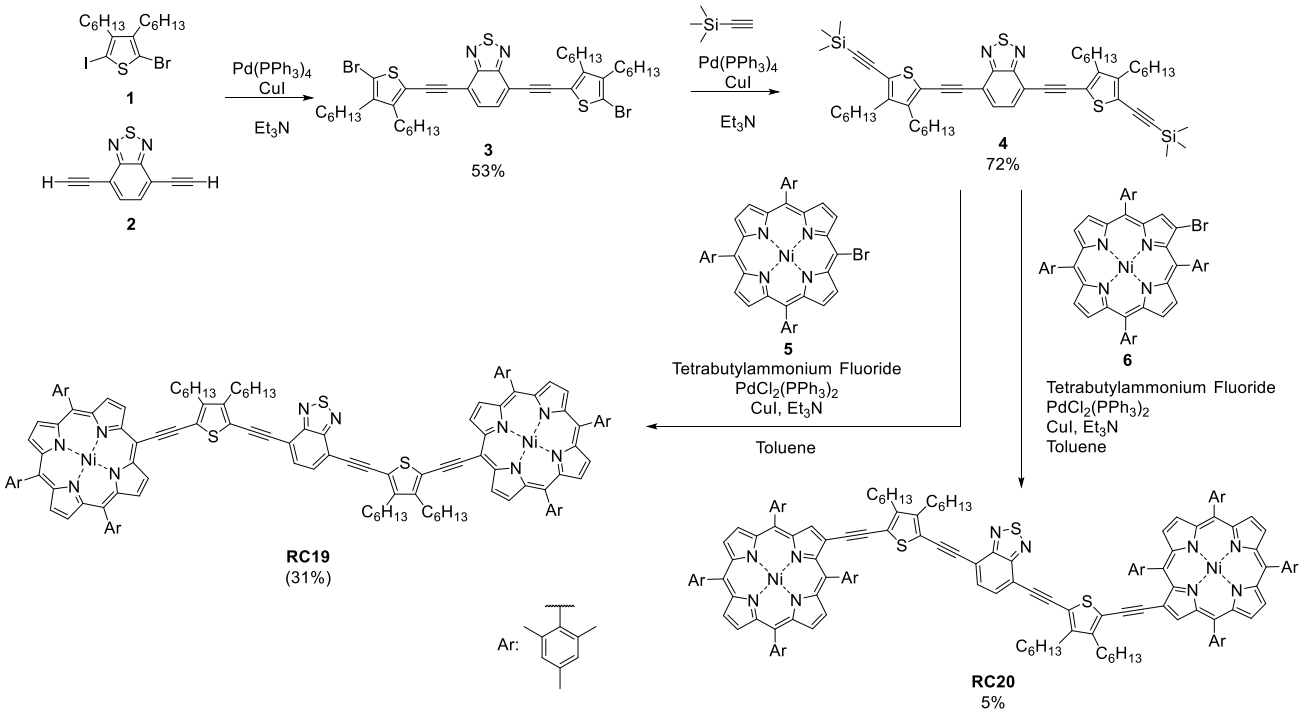

Scheme 1. Synthetic procedure for the synthesis of **RC19** and **RC20**.

The synthesis of D–A–Ds **RC19** and **RC20** involved a convergent method, and this is depicted in **Scheme 1**. 2-Bromo-3,4-dihexyl-5-iodothiophene (**1**)[62] was reacted with 4,7-diethynylbenzo[*c*]-1,2,5-thiadiazole (**2**)[63] under Sonogashira conditions to give **3** in 53% yield. The remaining bromo-substituents in the α-positions of the thiophene units were reacted with ethynyltrimethylsilane under Sonogashira coupling conditions to give **4** in 72% yield. The final D–A–Ds were obtained by in situ deprotection of the trimethylsilyl groups with tetrabutylammonium fluoride, followed by coupling with the corresponding Ni-porphyrin (**5** or **6**) under Sonogashira conditions. D–A–Ds **RC19** and **RC20** were obtained in 31% and 5% yield, respectively. Both D–A–Ds are soluble in common organic solvents and their purity was determined to be over 99% by high-performance liquid chromatography (see Figure S17 and S18 in Supporting Information). The target compounds were fully characterized by spectroscopic techniques and the spectra and synthetic procedures are provided in the Supporting Information.

2.2. Theoretical calculations

By using density functional theory at the B3LYP/6-31 G* calculation method (Gaussian 09), the most stable geometry, and the HOMO and LUMO levels of **RC19** and **RC20** were calculated and shown in Figure S19 and S20, Supporting Information. To reduce the computational cost, alkyl chains on the thiophene rings were changed by methyl groups. Both compounds show an almost planar geometry along the conjugated system, although the dihedral angle between the porphyrin macrocycle and the triple bond is lower for **RC19** (2.36°) than for **RC20** (6.80°). The higher planarity of **RC19** agrees with the more red-shifted maxima observed for **RC19** absorption spectrum.

Molecular orbital analysis of compound **RC19** reveals that the HOMO and LUMO orbitals are distributed throughout the entire conjugated system (Figure S19, Supporting Information). This suggests that the first singlet excited state (S_1) likely exhibits local excitation character, as the excitation does not lead to significant charge separation. In contrast, regarding compound **RC20** (Figure S20, Supporting Information), its HOMO orbital is also distributed along the entire conjugated system, while the LUMO is concentrated on the BTDZ unit. This indicates that upon excitation, a CT process occurs from the β-substituted porphyrins to the BTDA fragment, resulting in a CT character of the S_1 state.

2.3. Optical and Electrochemical Properties

The optical properties of **RC19** and **RC20** were studied in solid state (film, **Figure 2**a) and in chloroform solution at a concentration of 10^{-6} M (Figure S21, Supporting Information). The data are summarized in

Table 1. The main features in the spectra of the D–π–A–π–Ds are due to the Ni-porphyrin; in the case of **RC19**, the Soret band of the porphyrin is observed at 439 nm and one of the *Q*-bands appears at 546 nm. The absorbance of the BTDA and the thiophene spacers can be observed at 512 nm. A new band attributed to a CT process is observed at 607 nm due to the interaction of the porphyrins, the spacer, and the BTDA units. The same features are observed for **RC20**: the Soret band appears at 427 nm, one of the *Q*-bands at 536 nm, the BTDA-spacer unit at 509 nm, and, finally, the CT band appears at 586 nm. Comparison of the

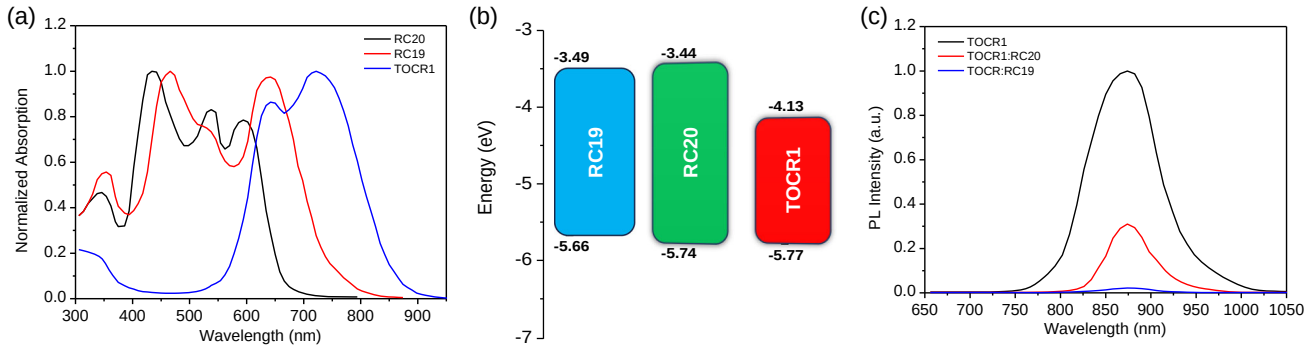

Figure 2. a) UV–vis absorption spectra (in film) of **RC19** and **RC20**; b) HOMO and LUMO energy levels of electron donors **RC19** and **RC20**, and electron acceptor TOCR1; and c) thin film PL spectra of pristine TOCR1 and its corresponding blends with **RC19** and **RC20**.

Table 1. Optical and electrochemical properties of **RC19** and **RC20**.

	λ_{max} [nm] (log ε)[a)]	λ_{max} [nm][b)]	E_g^{opt} [eV][c)]	E_{ox} [V][d)]	E_{red} [V][d)]	E_{HOMO} [eV][e)]	E_{LUMO} [eV][f)]	E_g^{eq} [eV][g)]
RC19	439 (5.40)	467	1.64	0.56	–	–5.66	–3.49	2.17
	512 (4.97)	526			1.61			
	546 (4.81)	630						
	607 (5.02)							
RC20	427 (5.44)	433	1.85	0.64	–	–5.74	–3.44	2.30
	536 (4.88)	539			1.66			
	586 (4.76)	591						

[a)]10^{-6} M in chloroform solution. [b)]Thin film spin-cast from dichloromethane solution. [c)]Optical bandgap determined from the λ_{onset} of the lower energy band of the absorption spectrum in film using the formula $E_g^{opt} = 1240/\lambda_{onset}$. [d)]Measured by OSWV: 5×10^{-4} M in ODCB-acetonitrile (4:1) versus Fc/Fc^+ glassy carbon, Pt counter electrode, 20 °C, 0.1 M Bu_4NClO_4, scan rate = 100 mV s^{-1}. [e)]Estimated from $E_{HOMO} = -5.1 - E^1_{ox}$. [f)]Estimated from $E_{LUMO} = -5.1 - E^1_{red}$. [g)]$E_g = E_{HOMO} - E_{LUMO}$.

absorption profiles of the two D–π–A–π–D systems shows that there are some differences, and these are attributed to effective conjugation along the backbone. For **RC19**, in which the porphyrin is linked by the meso-position, the absorption bands are shifted bathochromically and are wider when compared to those of **RC20**. Furthermore, the intensity of the CT band is markedly lower for **RC20**. The extent of the π-conjugation through the meso-position of the porphyrin leads to more changes than the conjugation through the β-position, with the latter compound being less effective for light harvesting purposes.

The thin film absorption spectra of these materials when cast from toluene are shown in Figure 2a. It can be observed that both porphyrins gave absorption spectra that are similar to those obtained in dichloromethane solution. Both porphyrins showed absorption spectra that are complementary to that of TOCR1, thus indicating that the BHJ active layer may harvest photons in the range from 300 nm to 910 nm. It can be seen that **RC19** presents an extensive bathochromic shift for all bands when compared to **RC20** and this is attributed to a more effective J-aggregation in the film. The optical bandgaps estimated from the absorption onsets in thin films are 1.64 and 1.85 eV for **RC19** and **RC20**, respectively. This trend is consistent with that obtained in the theoretical calculations.

The electrochemical properties of **RC19** and **RC20** were studied by cyclic and Osteryoung square-wave voltammetries (Table 1, Figure S23–S26, Supporting Information). Both compounds present reversible first oxidation and reduction potentials. In both cases, the first reduction potentials are attributed to the reduction of the BTDA where the LUMO level is located, as predicted in the theoretical calculations. The first oxidation potential in both D–A–Ds is attributed to the oxidation of the porphyrin macrocycle and this potential is lower for **RC19**. Thus, the HOMO/ LUMO energy levels were calculated to be −5.66 eV/−3.49 eV and −5.74 eV/−3.44 eV for **RC19** and **RC20**, respectively (Figure 2b). The HOMO–LUMO gaps are 2.17 eV for **RC19** and 2.30 eV for **RC20** and this follows the trend observed in the optical measurements.

The LUMO offsets between these porphyrins and TOCR1 are in the range 0.53–0.58 eV, which is higher than the driving force needed for the dissociation of excitons generated in the porphyrin phase of the BHJ active layer and subsequent electron transfer from the LUMO of the porphyrins to the LUMO of TOCR1. The HOMO offsets between TOCR1 and **RC19** and **RC20** are 0.11 and –0.01 eV, respectively.

The photoluminescence (PL) spectra of pristine TOCR1 and its blends with donors were recorded in order to obtain information about the dissociation of excitons generated in the TOCR1 acceptor phase of the BHJ active layer and subsequent hole transfer from the HOMO of TOCR1 to the HOMOs of donors. The resulting spectra are displayed in Figure 2c. Excitation of the pristine TOCR1 film at a wavelength of 720 nm gave rise to a PL peak at 874 nm and this was almost completely quenched for the TOCR1:**RC19** blend and only 70% quenched for the TOCR1:**RC20** blend. This observation demonstrates that there is efficient dissociation of excitons generated in the TOCR1 phase of TOCR1:**RC19** and subsequent transfer of holes from TOCR1 to **RC19** and that the dissociation of exciton generated in TOCR1 in TOCR1:**RC20** and subsequent hole transfer from TOCR1 to **RC20** is restricted in this active layer as the HOMO offset for TOCR1/**RC20** is lower than that for TOCR1/**RC19** (Figure 2c). Effective CT is possible in nonfullerene-based OSCs, even with low energy offsets between the donor and acceptors used in the BHJ active layers.

2.4. Photovoltaic Performance

The Ni-porphyrins **RC19** and **RC20** were employed as donors in conjunction with TOCR1 as the acceptor to build OSCs under ambient conditions. The OSCs were fabricated by depositing the BHJ active layer from toluene solutions and using the conventional ITO/PEDOT:PSS/active layer/PFN-Br/Al structure. The details and optimization of the device fabrication are described in the Supporting Information. In brief, the photovoltaic performance was initially optimized by varying the weight ratio between donor and acceptor. It was found that a donor: acceptor (1:1.2) active layer gave the best performance (Table S1 and Table S2, Supporting Information). The solvent additive approach (0.5% pyridine in toluene solvent) was then applied, and this led to a slight improvement in the photovoltaic performance. The thin film was then subjected to solvent vapor annealing (exposing the active layer to THF vapor for 40 s). The current–voltage (J–V) characteristics under illumination (AM1.5 G, 100 mW cm^{-2}) of the optimized OSCs are displayed in **Figure 3**a.

The OSCs based on **RC19** and **RC20** gave PCE values of 13.72% and 5.20%, respectively. **RC20** gave a V_{OC} of 0.98 V whereas **RC19** gave a value of 0.91 V. The higher value obtained for **RC20** may be a consequence of its deeper HOMO value when compared to **RC19** as the V_{OC} is directly related to the energy difference between the HOMO of the donor and LUMO of the acceptor. The J_{SC} and full factor (FF) values for the **RC19**-based OSCs are higher than for the **RC20** counterpart (**Table 2**)—a difference that may be due to the different external quantum efficiency (EQE) values for these devices. It can be seen from Figure 3b that the EQE values of **RC20**-based OSCs in the wavelength range 600–900 nm are lower than those at 300–600 nm. As the absorption of TOCR1 lies in the range of 600–900 nm, the excitons generated by the absorption of photons within this wavelength region are not fully dissociated into free charges and all of the holes are not transferred from the TOCR1 to **RC20** as the HOMO offset is not sufficient for these processes in the OSCs based on **RC20**. The EQE spectra of the OSCs closely resemble the corresponding absorption spectra of blended films (Figure S22, Supporting Information). The J_{SC} values estimated from the integration of the EQE spectra are 9.86 and 21.12 mA cm^{-2} for **RC20**- and **RC19**-based devices, respectively, and these values are in good agreement with those obtained from the J–V curves under illumination. The higher FF value obtained for **RC19**-based OSCs when compared to the **RC20** counterparts may be due to the different charge transport properties, which will be discussed later. The lower values of FF obtained compared to those reported in the literature for porphyrin-based devices[54] may be attributed to the fact that we fabricated the devices under ambient conditions, which can affect the charge transport in the devices. The higher V_{OC} for the OSCs based on **RC20**:TOCR1 is higher than that for the **RC19**:TOCR1, may be attributed to the deeper HOMO energy level of **RC20** as compared to **RC19**, because the V_{OC} of the OSCs based on BHJ active layer is linked with the energy difference between the HOMO of donor and LUMO of acceptor. Furthermore, the HOMO offset for **RC20**/TOCR1 is lower than that for **RC19**/TOCR1 (Figure 2b), which may reduce the energy loss in the OSCs.

Table 2. Photovoltaic data for the BHJ-OSCs based on donors **RC19** or **RC20** and TOCR1 as the acceptor.

Donor	J_{SC} [mA cm^{-2}]	V_{OC} [V]	FF	PCE [%]
RC19	21.36 (21.12)[a)]	0.91	0.706	13.72 (13.48)[b)]
RC20	10.02 (9.86)[a)]	0.98	0.53	5.20 (4.96)[b)]

[a)]Estimated from the integration of EQE spectra. [b)]Average of eight devices.

The photovoltaic performance of the OSCs depends on the generation of excitons and their dissociation into free charge carriers, charge transport through the active layer, and subsequent collection. As a consequence, the dependence of the photocurrent density (J_{ph}) on the effective voltage (V_{eff}) was analyzed[64,65] and the results are represented in **Figure 4**a.

Herein, $J_{ph} = J_L - J_D$, where J_L and J_D are the photocurrent under illumination and in the dark, respectively. $V_{eff} = V_o - V$, where V_o is the voltage at which J_{ph} is zero and V is the applied external bias voltage. In the case of the **RC19**-based device, J_{ph} approaches saturation (J_{sat}) at a V_{eff} greater than 1.5 V, which signifies complete exciton dissociation and charge collection. However, in the **RC20** counterpart, the J_{ph} does not saturate even

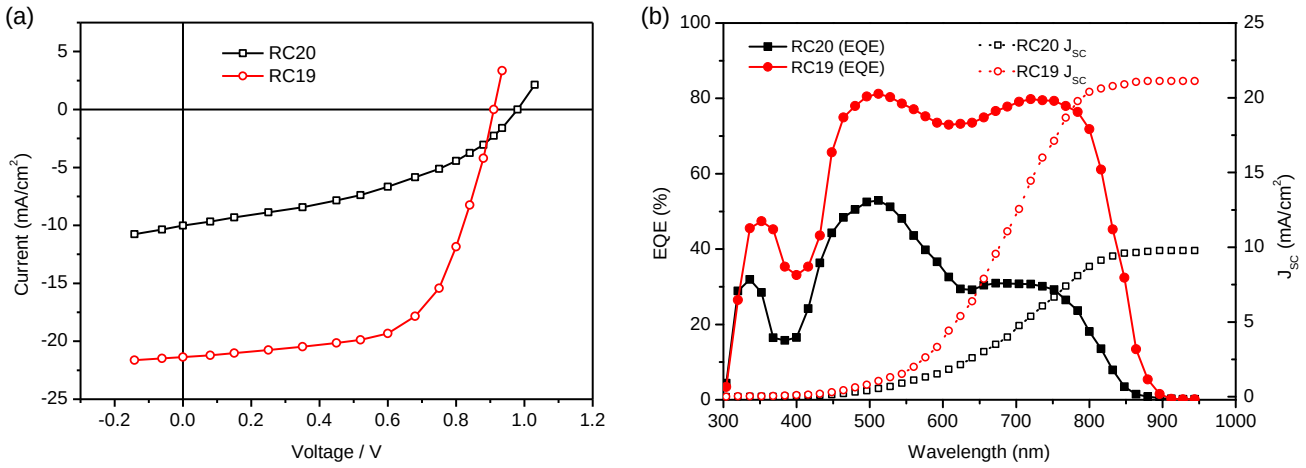

Figure 3. a) J–V curves and b) EQE and the integrated J_{SC} spectra of the studied binary systems (**RC19**:TOCR1 and **RC20**:TOCR1).

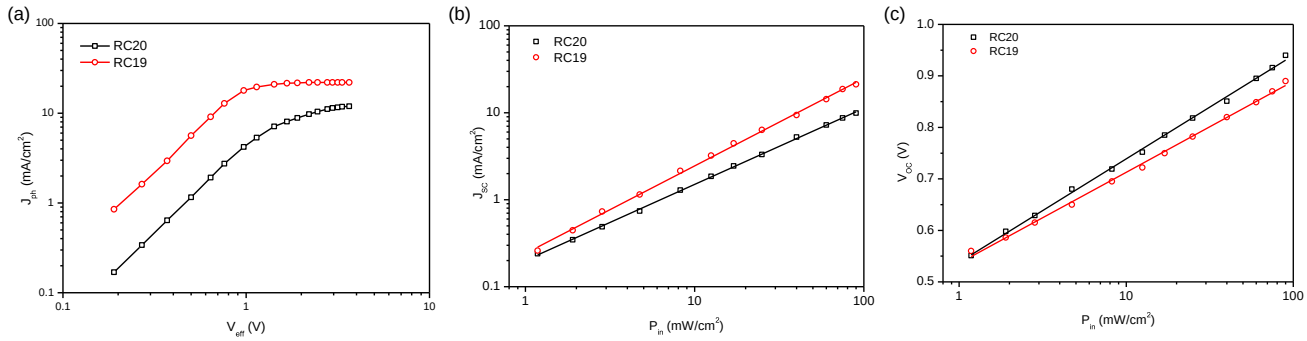

Figure 4. Variations of the binary blends **RC19**:TOCR1 and **RC20**:TOCR1: a) photocurrent density (J_{ph}) with effective voltage (V_{eff}); b) J_{SC} with illumination intensity (P_{in}); and c) V_{OC} with illumination intensity (P_{in}).

with a high V_{eff} of 3.5 V, thus indicating that the internal electric field is sufficient to achieve efficient exciton dissociation and charge transport. The exciton generation rate G_{max} is estimated as $G_{max} = J_{sat}/qL$, where L is the thickness of active layer and q is elementary charge. The G_{max} values are 1.27×10^{28} and 0.75×10^{28} m^{-3}s^{-1} for **RC19**- and **RC20**-based devices, respectively. The exciton dissociation probability (P_{diss}) and charge collection probability (P_{coll}) values are estimated as J_{ph}/J_{sat} under short-circuit conditions and maximum power point, respectively. The P_{diss}/P_{coll} values for **RC19**- and **R20**-based devices are calculated to be 0.972/0.745 and 0.76/0.62, respectively. These values indicate that the device based on **RC19** has more efficient exciton dissociation as well charge transport when compared to the **RC20** counterpart, as deduced from the higher FF value of the **RC19**-based OSC. Meanwhile, the low P_{diss} value obtained for the **RC20**-based device may be associated with the low HOMO offsets between TOCR1 and **RC20**, which restrict the dissociation of excitons generated in the TOCR1 phase and hole transfer from TOCR1 to **RC20**, thus resulting in low J_{SC} values for the **RC20**-based OSC.

The charge recombination in these devices was investigated by considering the variation of J_{SC} or V_{OC} with illumination intensity (P_{in}) (Figure 4b and Figure 4c).[66,67] The dependence of J_{SC} with P_{in} follows the power law equation $J_{SC} \propto (P_{in})^{\alpha}$, where exponent α gives information about the degree of bimolecular recombination. As shown in Figure 4b, the α values for the **RC19**- and **RC20**-based devices are 0.974 and 0.84, respectively. The α value for the **RC19** device is very close to unity and this is consistent with a low degree of bimolecular recombination and effective charge collection when compared to the **RC20** counterpart. The variation of V_{OC} with P_{in} is shown in Figure 4c and follows the equation $V_{OC} = (nkT/q)$ ln (P_{in}), where n, k, and T are the diode ideality factor, Boltzmann's constant, and temperature in Kelvin, respectively. The fitted slopes for the **RC19**- and **RC20**-based OSCs are 1.29 and 1.43, respectively, where a slope (n) close to unity indicates a low degree of trap-assisted charge recombination in the OSCs. These results suggest that both the bimolecular recombination and trap-assisted recombination processes are suppressed significantly in the **RC19**-based OSCs and this results in higher FF and J_{SC} values.

The transient photocurrent (TPC) and transient photovoltage (TPV) decay curves for these devices are shown in **Figure 5**a,b, respectively.[68,69]

The charge extraction times, as estimated from the exponential fitting of the TPC curve (Figure 5a), are 1.42 and 1.57 µs for **RC19** and **RC20**, respectively. The shorter charge extraction time for the **RC19**-based device suggests that faster charge transport occurs in this device when compared to the **RC20** counterpart. The photogenerated charge lifetimes estimated from the exponential decay of TPC are 6.71 and 4.67 µs, respectively, for **RC19**- and **RC20**-based devices and this indicates that charge recombination has been suppressed in the **RC19**-based OSC.

The hole and electron mobilities of the active layer were measured by fitting the dark J–V characteristic of hole-only and electron-only devices using the space charge limited current (see Figure 5c,d).[70,71] The hole mobility and electron mobility of the **RC19**:TOCR1 blend are calculated to be 2.92×10^{-4} cm^2 V s^{-1} and 3.67×10^{-4} cm^2 V s^{-1}, respectively (with an electron to hole mobility ratio of 1.27), both of which are higher than the values calculated for **RC20**:TOCR1 (hole and electron mobilities are 2.45×10^{-4} cm^2 V s^{-1} and 3.53 v 10^{-4} cm^2 V s^{-1} with an electron to hole mobility ratio of 1.44). The higher and more balanced hole and electron mobilities for the **RC19**:TOCR1 blend may originate from its faster charge sweep-out process, a possibility that is consistent with the TPC and TPV results and also with the FF values obtained for these devices. Moreover, the differences in FF values for these OSCs, as well as the series resistance (R_s) and shunt resistance (R_{sh}), were estimated from the J–V characteristics (Figure 3a and Table 2). It is apparent than the R_S value of the device based on **RC19** is lower than that for **RC20** and the R_{sh} value for **RC20** is higher than that for **RC19**, thus indicating more effective charge transport in the **RC19**-based device.

X-Ray diffraction (XRD) was employed to investigate the crystallization properties of the pristine **RC19** and **RC20** films (Figure S27, Supporting Information). It can be seen from Figure S27, Supporting Information that both **RC19** and **RC20** exhibit the same lamellar peak at $2\theta = 5.49°$ (with a d-spacing of 1.64 nm) in plane but they have different π–π stacking peaks, i.e., $2\theta = 24.67°$ (stacking distance = 0.361 nm) and 23.34° (stacking distance = 0.379) for **RC19** and **RC20**, respectively. The different π–π stacking peaks may be attributed to the different linking positions, i.e., the meso-position for **RC19** and β-position for **RC20**. After blending with TOCR1, the π–π stacking diffraction peaks are located at $2\theta = 24.53°$ and 23.43° for **RC19** and **RC20**, respectively (**Figure 6**a). The π–π stacking distance is shorter for the **RC19** blend (0.363 nm) as compared to

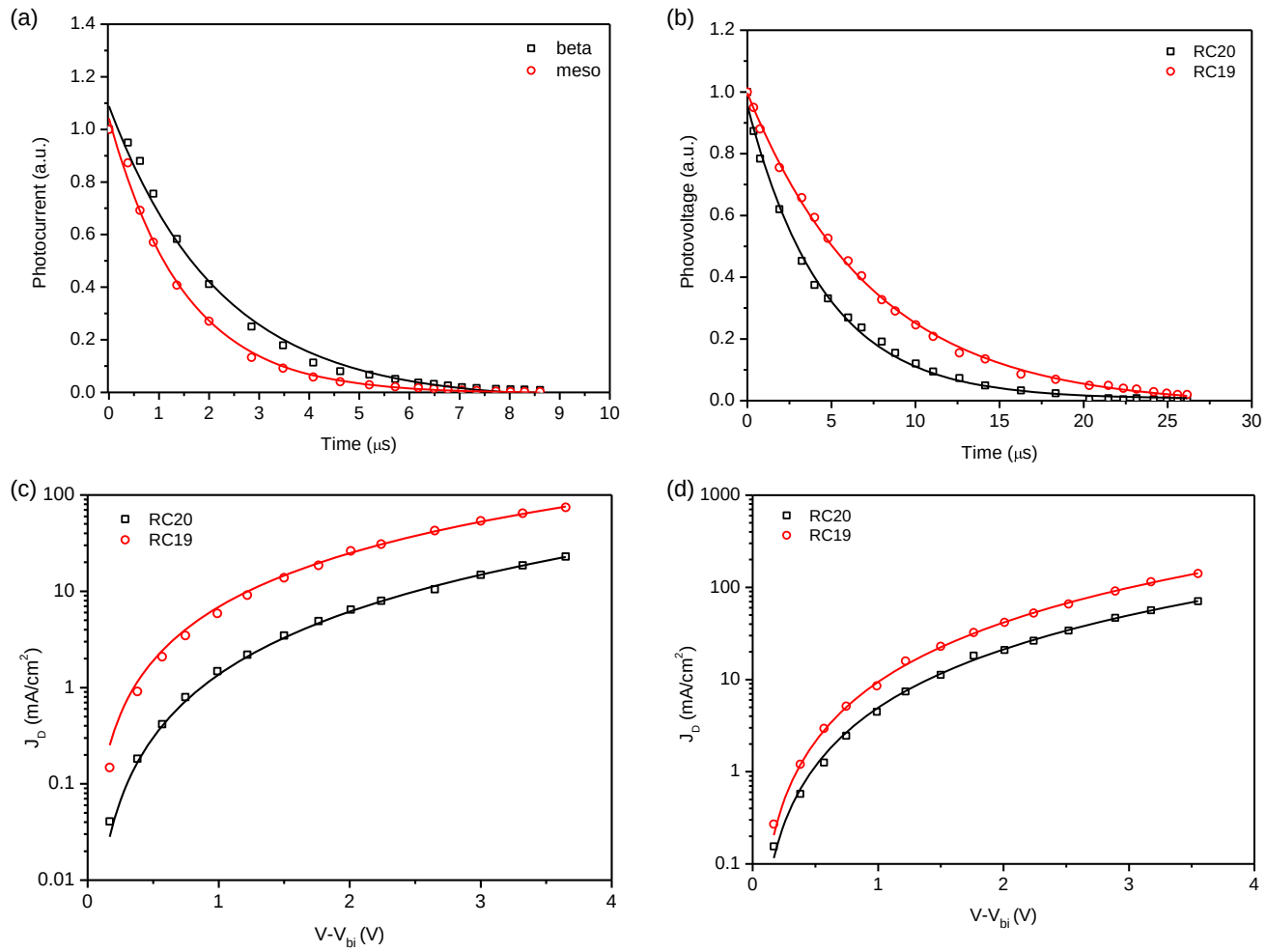

Figure 5. a) Charge extraction ability by TPC; b) charge recombination ability by TPV for the **RC19**- and **RC20**-based devices; dark *J*–*V* plots for hole c) and electron d) mobilities of the studied binary devices (**RC19**:TOCR1 and **RC20**:TOCR1).

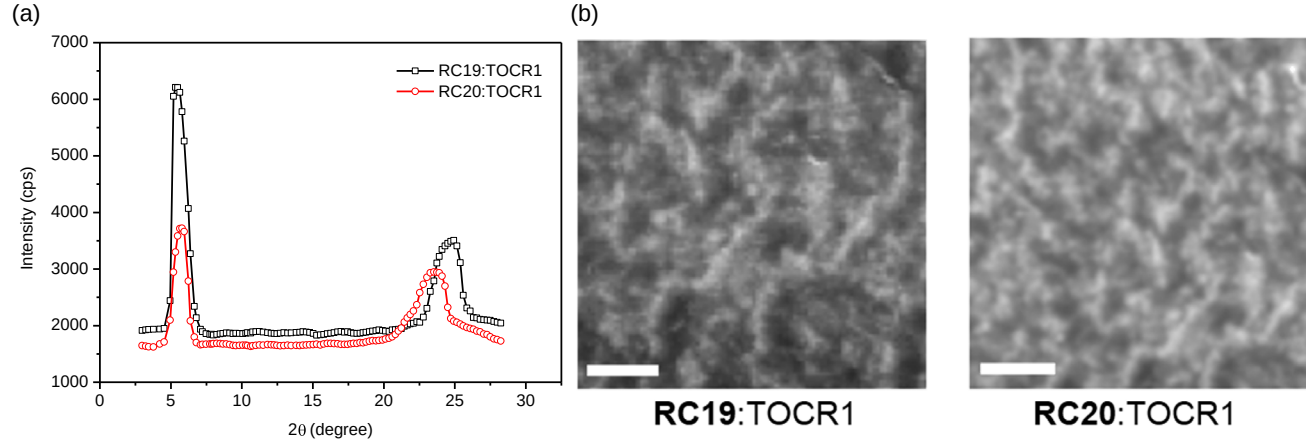

Figure 6. a) XRD patterns of the active layers (**RC19**:TOCR1 and **RC20**:TOCR1) and b) TEM images of **RC19** (b) and **RC20** (a) blends (scale bar: 100 nm).

RC20 (0.376 nm) and the crystal coherence length for the **RC19** blend is longer (3.72 nm) than that for **RC20** (2.82 nm). The smaller π–π stacking distance along with the larger CCL in the **RC19**:TOCR1 blended film is advantageous for charge transport and suppressed recombination processes—a situation in good agreement with the high FF and J_{SC} values for the **RC19**-based OSCs.

The morphologies of the active layers were examined by transmission electron microscopy (TEM) and the results are

represented in Figure 6b. It can be seen that both blends show a nanofiber morphology with a slightly more pronounced morphology for the **RC19**:TOCR1 blend. This leads to more efficient phase separation in this blend and this is beneficial for the suppression of recombination and, as a consequence, gives a higher FF.

3. Conclusion

Two D–π–A–π–D SMs have been designed and synthesized. The compounds are denoted as **RC19** and **RC20** and they contain the same BTDA acceptor core and Ni-porphyrin donor terminal units linked by thiophene π-linkers but with different linking positions, i.e., **RC19** (meso-position) and **RC20** (β-position). The effects of the linking position on the optical and electrochemical properties, as well as the molecular packing, were examined. It was found that the optical bandgap for **RC19** is lower than that for **RC20** with a deeper HOMO energy level for **RC20**. A low bandgap NFSMA, TOCR1, was employed to produce the optimized OSCs fabricated under ambient conditions. The devices based on **RC19** and **RC20** gave PCE values of 13.72% and 5.20%, respectively. The HOMO offset between **RC20** and TOCR1 is very small, and this hampers dissociation of excitons generated in TOCR1 and hole transfer from the TOCR1 to **RC20**, which result in a low photocurrent and a low PCE for these OSCs. The high PCE value obtained for **RC19** may be due to the higher photon harvesting ability of **RC19**:TOCR1, efficient exciton dissociation and T, balanced charge transport, and reduced bimolecular and trap-assisted recombination. **RC20** should be used as a donor in conjunction with acceptors that have a deeper HOMO energy level than **RC20**, so that more excitons in the acceptor can dissociate and more efficient CT can be attained. It should be noted that 13.72% represents the highest efficiency reported to date for binary OSCs based on porphyrins. Although **RC20** gave a low PCE on using TOCR1 as the acceptor, it can be used as donor with another appropriate acceptor with a deeper HOMO energy level than **RC20**, so that the exciton generated in that acceptor can be dissociated and subsequently hole can be transferred from acceptor to **RC20**.

4. Experimental Section

All synthetic details and characterization data for new donor materials and PSC device fabrication are provided in the Supporting Information. ^{1}H, ^{13}C NMR, MALDI-TOF absorption spectra, theoretical calculations, electrochemical and photovoltaic curves, and XRD data can be found in the Supporting Information.

Supporting Information

Supporting Information is available from the Wiley Online Library or from the author.

Acknowledgements

P.C. and F.L. thank Grants PID2019-105049RB-I00 and TED2021-131255B-C42 and RED2018-102815-T funded by MICIU/AEI/ 10.13039/501100011033 and, as appropriate, by "ERDF A way of making Europe," by "ERDF/EU," by the "European Union" or by the "European Union NextGenerationEU/PRTR," and SBPLY/21/180501/000142 funded by Junta de Comunidades de Castilla-La Mancha and European Social Funds. G.D.S. is thankful to the Department of Science and Technology for financial support.

Conflict of Interest

The authors declare no conflict of interest.

Data Availability Statement

The data that support the findings of this study are available on request from the corresponding author. The data are not publicly available due to privacy or ethical restrictions.

Keywords

all-small-molecule organic solar cells, meso-functionalization, porphyrins, power conversion efficiencies, β-functionalization

Received: January 24, 2024
Revised: March 7, 2024
Published online: April 9, 2024

[1] L. X. Chen, *ACS Energy Lett.* **2019**, *4*, 2537.
[2] F. Yang, Y. Huang, Y. Li, Y. Li, *npj Flex. Electron.* **2021**, *5*, 30.
[3] G. Zhang, F. R. Lin, F. Qi, T. Heumüller, A. Distler, H.-J. Egelhaaf, N. Li, P. C. Y. Chow, C. J. Brabec, A. K.-Y. Jen, H.-L. Yip, *Chem. Rev.* **2022**, *122*, 14180.
[4] W. Lowrie, R. J. E. Westbrook, J. Guo, H. I. Gonev, J. Marin-Beloqui, T. M. Clarke, *J. Chem. Phys.* **2023**, *158*, 110901.
[5] B. Zhang, F. Yang, Y. Li, *Small Sci.* **2023**, *3*, 2300004.
[6] H. Yao, J. Hou, *Angew. Chemie Int. Ed.* **2022**, *61*, e202209021.
[7] J. Yuan, Y. Zhang, L. Zhou, G. Zhang, H.-L. Yip, T.-K. Lau, X. Lu, C. Zhu, H. Peng, P. A. Johnson, M. Leclerc, Y. Cao, J. Ulanski, Y. Li, Y. Zou, *Joule* **2019**, *3*, 1140.
[8] S. Li, C.-Z. Li, M. Shi, H. Chen, *ACS Energy Lett.* **2020**, *5*, 1554.
[9] J. Yuan, Y. Zou, *Org. Electron.* **2022**, *102*, 106436.
[10] Y. Yang, *ACS Nano* **2021**, *15*, 18679.
[11] B. Lu, J. Wang, Z. Zhang, J. Wang, X. Yuan, Y. Ding, Y. Wang, Y. Yao, *Nano Sel.* **2021**, *2*, 2029.
[12] Q. Wei, J. Yuan, Y. Yi, C. Zhang, Y. Zou, *Natl. Sci. Rev.* **2021**, *8*, nwab121.
[13] L. Wang, Q. An, L. Yan, H.-R. Bai, M. Jiang, A. Mahmood, C. Yang, H. Zhi, J.-L. Wang, *Energy Environ. Sci.* **2022**, *15*, 320.
[14] X. Zhao, Q. An, H. Zhang, C. Yang, A. Mahmood, M. Jiang, M. H. Jee, B. Fu, S. Tian, H. Y. Woo, Y. Wang, J.-L. Wang, *Angew. Chemie Int. Ed.* **2023**, *62*, e202216340.
[15] L. Zhu, M. Zhang, J. Xu, C. Li, J. Yan, G. Zhou, W. Zhong, T. Hao, J. Song, X. Xue, Z. Zhou, R. Zeng, H. Zhu, C.-C. Chen, R. C. I. MacKenzie, Y. Zou, J. Nelson, Y. Zhang, Y. Sun, F. Liu, *Nat. Mater.* **2022**, *21*, 656.
[16] C. Han, J. Wang, S. Zhang, L. Chen, F. Bi, J. Wang, C. Yang, P. Wang, Y. Li, X. Bao, *Adv. Mater.* **2023**, *35*, 2208986.
[17] G. Wu, X. Xu, C. Liao, L. Yu, R. Li, Q. Peng, *Small* **2023**, *19*, 2302127.
[18] Y. Wei, Z. Chen, G. Lu, N. Yu, C. Li, J. Gao, X. Gu, X. Hao, G. Lu, Z. Tang, J. Zhang, Z. Wei, X. Zhang, H. Huang, *Adv. Mater.* **2022**, *34*, 2204718.

[19] J. Fu, P. W. K. Fong, H. Liu, C.-S. Huang, X. Lu, S. Lu, M. Abdelsamie, T. Kodalle, C. M. Sutter-Fella, Y. Yang, G. Li, *Nat. Commun.* **2023**, *14*, 1760.
[20] M. Xiao, L. Liu, Y. Meng, B. Fan, W. Su, C. Jin, L. Liao, F. Yi, C. Xu, R. Zhang, A. K.-Y. Jen, W. Ma, Q. Fan, *Sci. China Chem.* **2023**, *66*, 1500.
[21] G. Ding, T. Chen, M. Wang, X. Xia, C. He, X. Zheng, Y. Li, D. Zhou, X. Lu, L. Zuo, Z. Xu, H. Chen, *Nano-Micro Lett.* **2023**, *15*, 92.
[22] L. Meng, H. Liang, G. Song, M. Li, Y. Huang, C. Jiang, K. Zhang, F. Huang, Z. Yao, C. Li, X. Wan, Y. Chen, *Sci. China Chem.* **2023**, *66*, 808.
[23] Z. Zheng, J. Wang, P. Bi, J. Ren, Y. Wang, Y. Yang, X. Liu, S. Zhang, J. Hou, *Joule* **2022**, *6*, 171.
[24] M. Shi, T. Wang, Y. Wu, R. Sun, W. Wang, J. Guo, Q. Wu, W. Yang, J. Min, *Adv. Energy Mater.* **2021**, *11*, 2002709.
[25] N. Zhou, A. S. Dudnik, T. I. N. G. Li, E. F. Manley, T. J. Aldrich, P. Guo, H.-C. Liao, Z. Chen, L. X. Chen, R. P. H. Chang, A. Facchetti, M. Olvera de la Cruz, T. J. Marks, *J. Am. Chem. Soc.* **2016**, *138*, 1240.
[26] L. Sun, X. Xu, S. Song, Y. Zhang, C. Miao, X. Liu, G. Xing, S. Zhang, *Macromol. Rapid Commun.* **2019**, *40*, 1900074.
[27] Y. Lin, Y. Li, X. Zhan, *Chem. Soc. Rev.* **2012**, *41*, 4245.
[28] H. Gao, Y. Sun, L. Meng, C. Han, X. Wan, Y. Chen, *Small* **2023**, *19*, 2205594.
[29] B. Kan, Y. Kan, L. Zuo, X. Shi, K. Gao, *InfoMat* **2021**, *3*, 175.
[30] W. Ye, Y. Yang, Z. Zhang, Y. Zhu, L. Ye, C. Miao, Y. Lin, S. Zhang, *Sol. RRL* **2020**, *4*, 2000258.
[31] Z. Zhang, Y. Wang, C. Sun, Z. Liu, H. Wang, L. Xue, Z.-G. Zhang, *Nano Sel.* **2022**, *3*, 233.
[32] H.-F. Zhi, M. Jiang, H. Zhang, Q. An, H.-R. Bai, M. H. Jee, H. Y. Woo, D. Li, X. Huang, J.-L. Wang, *Adv. Funct. Mater.* **2023**, *33*, 2300878.
[33] J. L. Wang, K. K. Liu, J. Yan, Z. Wu, F. Liu, F. Xiao, Z. F. Chang, H. Bin Wu, Y. Cao, T. P. Russell, *J. Am. Chem. Soc.* **2016**, *138*, 7687.
[34] L. Nian, Y. Kan, K. Gao, M. Zhang, N. Li, G. Zhou, S. B. Jo, X. Shi, F. Lin, Q. Rong, F. Liu, G. Zhou, A. K.-Y. Jen, *Joule* **2020**, *4*, 2223.
[35] Y. Sun, L. Nian, Y. Kan, Y. Ren, Z. Chen, L. Zhu, M. Zhang, H. Yin, H. Xu, J. Li, X. Hao, F. Liu, K. Gao, Y. Li, *Joule* **2022**, *6*, 2835.
[36] J. Qin, Z. Chen, P. Bi, Y. Yang, J. Zhang, Z. Huang, Z. Wei, C. An, H. Yao, X. Hao, T. Zhang, Y. Cui, L. Hong, C. Liu, Y. Zu, C. He, J. Hou, *Energy Environ. Sci.* **2021**, *14*, 5903.
[37] Z. Li, X. Wang, N. Zheng, A. Saparbaev, J. Zhang, C. Xiao, S. Lei, X. Zheng, M. Zhang, Y. Li, B. Xiao, R. Yang, *Energy Environ. Sci.* **2022**, *15*, 4338.
[38] K. Ma, W. Feng, H. Liang, H. Chen, Y. Wang, X. Wan, Z. Yao, C. Li, B. Kan, Y. Chen, *Adv. Funct. Mater.* **2023**, *33*, 2214926.
[39] M. Jiang, H.-F. Zhi, B. Zhang, C. Yang, A. Mahmood, M. Zhang, H. Y. Woo, F. Zhang, J.-L. Wang, Q. An, *ACS Energy Lett.* **2023**, *8*, 1058.
[40] L. Zhang, R. Sun, Z. Zhang, J. Zhang, Q. Zhu, W. Ma, J. Min, Z. Wei, D. Deng, *Adv. Mater.* **2022**, *34*, 2207020.
[41] A. Mahmood, J.-Y. Hu, B. Xiao, A. Tang, X. Wang, E. Zhou, *J. Mater. Chem. A* **2018**, *6*, 16769.
[42] V. Piradi, F. Yan, X. Zhu, W.-Y. Wong, *Mater. Chem. Front.* **2021**, *5*, 7119.
[43] J. Kesters, P. Verstappen, M. Kelchtermans, L. Lutsen, D. Vanderzande, W. Maes, *Adv. Energy Mater.* **2015**, *5*, 1500218.
[44] K. Gao, Y. Kan, X. Chen, F. Liu, B. Kan, L. Nian, X. Wan, Y. Chen, X. Peng, T. P. Russell, Y. Cao, A. K.-Y. Jen, *Adv. Mater.* **2020**, *32*, 1906129.
[45] V. Piradi, X. Xu, H. Yin, J. K. W. Ho, F. Yan, Q. Peng, S. K. So, X. Zhu, *Energy Technol.* **2022**, *10*, 2100908.
[46] V. Piradi, X. Xu, Z. Wang, J. Ali, Q. Peng, F. Liu, X. Zhu, *ACS Appl. Mater. Interfaces* **2019**, *11*, 6283.
[47] V. Piradi, X. Xu, Q. Peng, X. Zhu, *Mater. Adv.* **2020**, *1*, 2520.
[48] V. Cuesta, R. Singhal, P. de la Cruz, G. D. Sharma, F. Langa, *ACS Appl. Mater. Interfaces* **2019**, *11*, 7216.
[49] Y. Gao, V. Piradi, X. Zhu, S. K. So, *ACS Appl. Energy Mater.* **2022**, *5*, 4916.
[50] V. Cuesta, M. K. Singh, E. Gutierrez-Fernandez, J. Martín, R. Domínguez, P. de la Cruz, G. D. Sharma, F. Langa, *ACS Appl. Mater. Interfaces* **2022**, *14*, 11708.
[51] V. Cuesta, R. Singhal, P. Cruz, G. D. Sharma, F. Langa, *ChemSusChem* **2021**, *14*, 3494.
[52] V. Cuesta, M. Vartanian, P. de la Cruz, R. Singhal, G. D. Sharma, F. Langa, *J. Mater. Chem. A* **2017**, *5*, 1057.
[53] V. Piradi, Y. Gao, F. Yan, M. Imran, J. Zhao, X. Zhu, S. K. So, *ACS Appl. Energy Mater.* **2022**, *5*, 7287.
[54] K. Gao, S. B. Jo, X. Shi, L. Nian, M. Zhang, Y. Kan, F. Lin, B. Kan, B. Xu, Q. Rong, L. Shui, F. Liu, X. Peng, G. Zhou, Y. Cao, A. K. Y. Jen, *Adv. Mater.* **2019**, *31*, 1807842.
[55] Q. Bei, B. Zhang, K. Wang, S. Zhang, G. Xing, C. Cabanetos, *Chinese Chem. Lett.* **2023**, 108438.
[56] Q. Nie, A. Tang, Q. Guo, E. Zhou, *Nano Energy* **2021**, *87*, 106174.
[57] P. Cong, Z. Wang, Y. Geng, Y. Meng, C. Meng, L. Chen, A. Tang, E. Zhou, *Nano Energy* **2023**, *105*, 108017.
[58] Y. Zhang, J. Song, J. Qu, P.-C. Qian, W.-Y. Wong, *Sci. China Chem.* **2021**, *64*, 341.
[59] M. Vartanian, R. Singhal, P. de la Cruz, G. D. Sharma, F. Langa, *Chem. Commun.* **2018**, *54*, 14144.
[60] V. Cuesta, R. Singhal, P. Cruz, G. D. Sharma, F. Langa, P. de la Cruz, G. D. Sharma, F. Langa, P. Cruz, G. D. Sharma, F. Langa, *ChemSusChem* **2021**, *14*, 3494.
[61] M. Privado, B. Donoso, K. Khandelwal, R. Singhal, F. G. Guijarro, Á. Díaz-Ortíz, P. Prieto, P. de la Cruz, G. D. Sharma, F. Langa, *J. Mater. Chem. C* **2022**, *10*, 13174.
[62] R. Tkachov, V. Senkovskyy, H. Komber, A. Kiriy, *Macromolecules* **2011**, *44*, 2006.
[63] X. Cheng, H. Lian, L. Yao, W. Xia, J. Han, J. Fan, Q. Dong, W.-Y. Wong, *Appl. Surf. Sci.* **2022**, *599*, 153877.
[64] S. R. Cowan, A. Roy, A. J. Heeger, *Phys. Rev. B* **2010**, *82*, 245207.
[65] P. W. M. Blom, V. D. Mihailetchi, L. J. A. Koster, D. E. Markov, *Adv. Mater.* **2007**, *19*, 1551.
[66] A. K. K. Kyaw, D. H. Wang, D. Wynands, J. Zhang, T.-Q. Nguyen, G. C. Bazan, A. J. Heeger, *Nano Lett.* **2013**, *13*, 3796.
[67] L. J. A. Koster, V. D. Mihailetchi, R. Ramaker, P. W. M. Blom, *Appl. Phys. Lett.* **2005**, *86*, 123509.
[68] S. Wood, J. C. Blakesley, F. A. Castro, *Phys. Rev. Appl.* **2018**, *10*, 24038.
[69] X. Xu, J. Xiao, G. Zhang, L. Wei, X. Jiao, H.-L. Yip, Y. Cao, *Sci. Bull.* **2020**, *65*, 208.
[70] C. M. Proctor, C. Kim, D. Neher, T.-Q. Q. Nguyen, *Adv. Funct. Mater.* **2013**, *23*, 3584.
[71] M. Sajedi Alvar, P. W. M. Blom, G.-J. A. H. Wetzelaer, *Nat. Commun.* **2020**, *11*, 4023.